Available online at www.sciencedirect.com
ScienceDirect
Continental Shelf Research 27 (2007) 1980–1999
CONTINENTAL SHELF RESEARCH
www.elsevier.com/locate/csr

Early spring turbulent mixing in an ice-covered Arctic fjord during transition to melting

Ilker Fer[a,*], Karolina Widell[a,b]

[a]*Bjerknes Centre for Climate Research and Geophysical Institute, University of Bergen, Allégaten 70, N-5007 Bergen, Norway*
[b]*University Centre in Svalbard, Longyearbyen, Norway*

Received 27 March 2006; received in revised form 3 April 2007; accepted 18 April 2007
Available online 27 April 2007

Abstract

Observations are presented of currents, hydrography and turbulence in a jet-type tidally forced fjord in Svalbard. The fjord was ice covered at the time of the experiment in early spring 2004. Turbulence measurements were conducted by both moored instruments within the uppermost 5 m below the ice and a microstructure profiler covering 3–60 m at 75 m depth. Tidal choking at the mouth of the fjord induces a tidal jet advecting relatively warmer water past the measurement site and dominating the variability in hydrography. While there was no strong correlation with the observed hydrography or mixing and the phase of the semidiurnal tidal cycle, the mean structure in dissipation of turbulent kinetic energy, work done under the ice and the mixing in the water column correlated with the current when conditionally sampled for tidal jet events. Observed levels of dissipation of turbulent kinetic energy per unit mass, $1.1\times10^{-7}\,\mathrm{W\,kg^{-1}}$, and eddy diffusivity, $7.3\times10^{-4}\,\mathrm{m^2\,s^{-1}}$, were comparable to direct measurements at other coastal sites and shelves with rough topography and strong forcing. During spring tides, an average upward heat flux of $5\,\mathrm{W\,m^{-2}}$ in the under-ice boundary layer was observed. Instantaneous (1 h averaged) large heat flux events were correlated with periods of large inflow, hence elevated heat fluxes were associated with the tidal jet and its heat content. Vertical heat fluxes are derived from shear-probe measurements by employing a novel model for eddy diffusivity [Shih et al., 2005. Parameterization of turbulent fluxes and scales using homogeneous sheared stably stratified turbulence simulations. Journal of Fluid Mechanics 525, 193–214]. When compared to the direct heat flux measurements using the eddy correlation method at 5 m below the ice, the upper 4–6 m averaged heat flux estimates from the microstructure profiler agreed with the direct measurements to within 10%. During the experiment water column was stably, but weakly, stratified. Destabilizing buoyancy fluxes recorded close to the ice were absent at 5 m below the ice, and overall, turbulence production was dominated by shear. A scaling for dissipation employing production by both stress and buoyancy [Lombardo and Gregg, 1989. Similarity scaling of viscous and thermal dissipation in a convecting boundary layer. Journal of Geophysical Research 94, 6273–6284] was found to be appropriate for the under-ice boundary layer.

Keywords: Mixing; Turbulence; Fast ice; Fjords; Arctic; Svalbard; Van Mijenfjorden

1. Introduction

During winter and early spring, the surface ice cover over seasonally frozen Arctic fjords prevents

*Corresponding author. Tel.: +47 5558 2580; fax: +47 5558 9883.
E-mail address: Ilker.Fer@gfi.uib.no (I. Fer).

0278-4343/$ - see front matter © 2007 Elsevier Ltd. All rights reserved.
doi:10.1016/j.csr.2007.04.003

energy input from the wind and low run-off significantly reduces the estuarine circulation. Remaining major sources of energy for mixing are convection induced by salt rejection from the ice, the response to the atmospheric disturbances in the ice-free coastal waters at the entrance to the fjord, and the tidal motions. In a sill fjord, the energy can be extracted from the barotropic tide through processes including friction against boundaries, baroclinic wave drag, tidal jets and high-frequency internal waves (Farmer and Freeland, 1983; Stigebrandt and Aure, 1989). The progressive internal waves generated at a sill can break at the sloping sides of a fjord contributing to the vertical mixing of the fjord basin (Stigebrandt, 1976). Tidal jets occur when the constriction at the mouth of a fjord is such that the tidal flow is too fast for internal wave generation. Inall et al. (2004) reported on the energy budget of a jet-type fjord, where 16% of the incident barotropic tidal energy was extracted. During neap tides, the fjord was favorable to internal wave generation and the loss due to baroclinic wave drag increased by three fold relative to during spring tides. The transfer processes governing the vertical distribution of mass, heat, and momentum are crucial for deep water renewal, nutrient transfer into the surface layer and, in ice-covered fjords, for heat supply towards the ice.

The sea ice provides a stable platform from which highly accurate oceanic turbulence flux measurements can be made using eddy-correlation methods. Such experiments were conducted in the past three decades following the seminal work of McPhee and Smith (1976) contributing to our understanding of the under-ice boundary layer and the oceanic boundary layer, in general. Such direct flux measurements are rare in the ice-free ocean (Fleury and Lueck, 1994; Moum, 1996). Instead, fluxes are inferred from shear, conductivity or temperature variances resolved at dissipation scales by sensors mounted on profiling or towed instruments (Gregg, 1987; Moum et al., 2002) or on manned or autonomous underwater vehicles (Osborn and Lueck, 1985; Fer et al., 2002; Thorpe et al., 2003) and using challengeable assumptions (e.g. isotropy, homogeneity, simplification of turbulent budget equations).

The majority of under-ice turbulence measurements were conducted from drifting pack-ice (e.g., McPhee, 1992; McPhee and Martinson, 1994; McPhee and Stanton, 1996) under conditions covering near-neutral, stabilizing and destabilizing surface fluxes. Studies from land-fast ice (fast ice, hereinafter) were made in the Canadian Arctic, e.g. in Resolute Passage (Shirasawa and Ingram, 1997), in Hudson Bay (Shirasawa and Ingram, 1991), and in Barrow Strait at ~160 m water depth (Crawford et al., 1999), as well as from an artificially constructed growing thin sea ice pool in Saromo-ko Lagoon in Japan (Shirasawa et al., 1997). Among the relevant work, only McPhee and Stanton (1996) and Crawford et al. (1999) obtained both types of oceanic turbulence measurement: (1) time series of direct turbulent fluxes at several vertical levels under the ice (2) vertical profiles of turbulent structure through microstructure shear and/or temperature. Here we report on measurements of both types under fast ice in a tidally active Arctic fjord at a depth of about 75 m, much shallower than the site studied by Crawford et al. (1999). Following Turner (1973), who differentiated between "external mixing" induced by surface and bottom generated turbulence and "internal mixing" induced by processes typically in the pycnocline away from the boundaries, we might expect the external and internal mixing to interact and cover a much larger portion of the water column compared to deeper waters. The level of mixing across the pycnocline is particularly important in supplying nutrient rich water into the surface layer as well as for supplying heat towards the ice contributing to its thermodynamic balance (Sundfjord et al., 2007).

Due to their accessibility and relatively stable ice conditions, Arctic fjords offer suitable laboratories for studies on first year sea ice. The field experiment described here was conducted in Van Mijenfjorden in the Svalbard archipelago as part of an atmosphere–ice–ocean interaction study aiming at processes that govern the growth and decay of sea ice. The focus of this paper is to describe the oceanographic context throughout the experiment, report on nearly full water column turbulence observations, identify processes responsible for mixing and compare microstructure profile and eddy-correlation measurements in early spring 2004.

The structure of the paper is as follows. We describe the site and experiments in Section 2, together with the data sampling and reduction processes for different types of turbulence measurement. The oceanic background including tides, currents and the hydrography during the time of the observations are given in Section 3. The mixing in the water column, heat fluxes under the ice and evolution in a tidal cycle are described in Section 4.

Discussion in Section 5 addresses eddy diffusivity estimates and comparison with other work conducted under-ice, in the ice-free open ocean and on shelves. Summary and concluding remarks are given in Section 6.

2. Experimental methods and data reduction

2.1. Experiment

The experiment was conducted over the ice-covered Van Mijenfjorden located on the island of Spitsbergen in the Svalbard archipelago (Fig. 1). The 110 m deep fjord is about 68 km long and 10 km wide. Observations were made for 18 days from 11 March 2004 at a station established over 1.2 m thick, undeformed ice on the 75 m isobath, about 10 km from the mouth of the fjord, which is partially blocked by an island.

During the experiment the atmospheric conditions were relatively mild and the ice gradually warmed, with a heat conduction of about 6 W m^{-2} in the lower part of the ice inferred from the vertical temperature gradient measured by thermistors embedded in the ice (Widell et al., 2006). The melting season typically begins in May–June.

The instrumentation deployed comprised two Aanderaa current metres (RCM) nominally at 10 and 50 m below the ice, two sets of turbulence instrument clusters (TIC, Section 2.2) nominally at 1 and 5 m below the ice and a microstructure profiler (MSS, Section 2.3) profiling between about 3 m under the ice to 60 m depth. The RCMs sampled the horizontal current every 10 min between 12 and 29 March 2004. The three sets of data used in this study were collected from hydroholes approximately forming a triangle with sides 40 m (MSS–TIC), 130 m (RCM–TIC), and 120 m (MSS–RCM), with MSS station located at 77° 42.998′N and 15° 10.46′E (see the inset in Fig. 1). The bulk of the data presented is from 21 to 29 March when MSS was deployed. The time convention used is such that day of year (doy) 0.5 corresponds to UTC noon at 1 January 2004 and 21 March 2004 starts at doy = 80. A more detailed account on the complete TIC record is presented in Widell (2006).

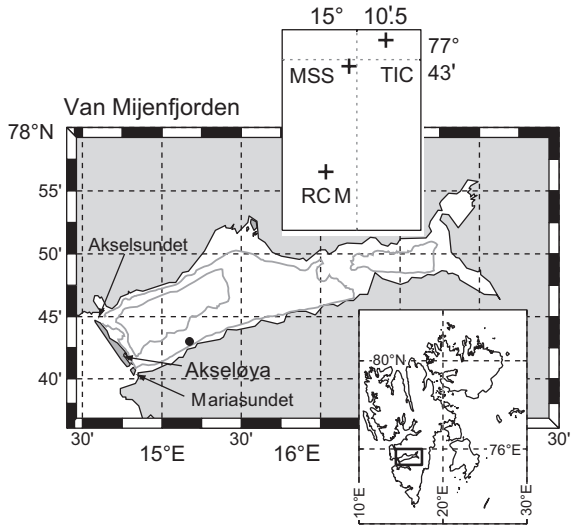

Fig. 1. Location map of Van Mijenfjorden together with the shore line, 50 and 100 m isobaths and place names mentioned in the text. The bullet marks the position of the ice station. The insets show (bottom) the Svalbard archipelago with a rectangle showing Van Mijenfjorden, (top) the location of TIC, MSS and RCM measurements.

2.2. Moored turbulence measurement and processing details

Time series of temperature, T, conductivity, C, and three orthogonal components of velocity were acquired and averaged at 2 Hz by instruments clustered at nominally 1 and 5 m below the ice. In addition to the slow time-response but relatively accurate conductivity units (SBE4C) installed at both levels, a fast-response dual-needle conductivity sensor (SBE7) was mounted at 1 m. Temperature and 3D velocity were measured at approximately the same point by fast-response SBE3F sensors and 5 MHz SonTek ADVOcean Doppler current meters.

Salinity, S, is calculated in practical salinity units (psu) using the measured T, C, and pressure at the measurement level. Turbulent fluxes are calculated at 15 min intervals by the eddy-correlation method. The 15 min averaging interval is chosen to be sufficiently larger than the time scale of the largest energy containing eddies in the under-ice boundary layer. At each segment the velocity components are aligned with the streamline such that u, v, and w are the longitudinal, transverse and vertical (positive upwards) components and $\langle v \rangle$ and $\langle w \rangle$ vanish. Here and in the following angle brackets denote averaging.[1] Fluctuating quantities, denoted by prime, are obtained by linearly detrending each

[1]Throughout the paper $\langle \cdot \rangle$ is used interchangeably denoting MSS-set averages, survey-means, 15-min averaged TIC-derived properties. The context is made clear in the text.

segment. Fluxes are obtained by zero-lag covariances assuming eddies advected past the sensors over the averaging time are representative of the ensemble of instantaneous turbulent fields (Taylor's frozen turbulence hypothesis). Turbulent heat flux is $F_H = \rho C_P \langle w'T' \rangle$, in units of Wm^{-2}, where ρ is the density and C_P is the specific heat of seawater. Reynolds stress per unit mass is $\vec{\tau} = \langle u'w' \rangle + i\langle v'w' \rangle$, expressed in complex notation where $i = (-1)^{1/2}$, and local friction speed is $u_* = |\vec{\tau}|^{1/2}$. The salinity flux $F_S = \langle w'S' \rangle$, in units of psu $m\,s^{-1}$, is resolved only at 1 m below the ice where the fast-response conductivity sensor was mounted. The low-response conductivity units do not sufficiently resolve the inertial subrange and underestimate salt fluxes by typically 25% (McPhee and Stanton, 1996). F_S is sensitive to the absolute salinity and is calculated after careful in situ calibration of the fast-response conductivity sensor. The calibration is conducted, as detailed in Widell et al. (2006), every 15 min against the relatively accurate SBE4C. The dissipation rate of turbulent kinetic energy per unit mass, ε, is calculated from the inertial subrange of the vertical velocity wavenumber spectrum (using Taylor's hypothesis frequency is converted to wavenumber) using the Kolmogorov relationship as described in McPhee (2002).

2.3. Turbulence profiler measurement and processing details

The microstructure data were collected at 1024 Hz using a loosely tethered free-fall MSS profiler (Prandke and Stips, 1998) equipped with airfoil shear probes and fast-response conductivity and temperature (FP07) sensors. The profiler comprises an acceleration sensor and conventional conductivity–temperature–depth (CTD) sensors for precision measurements. Microstructure data are processed as described in Fer (2006). The dissipation rate of turbulent kinetic energy per unit mass, ε in units $W\,kg^{-1}$, is calculated using the isotropic relation $\varepsilon = 7.5\nu\langle u_z^2 \rangle$, where ν is the viscosity of seawater ($\sim 1.9 \times 10^{-6}\,m^2\,s^{-1}$ for the cold temperatures recorded in this study), and u_z is the shear of the horizontal small-scale velocity. The instrument fall speed ($\sim 0.6\,m\,s^{-1}$) is used to convert from frequency domain to vertical wavenumber domain using Taylor's hypothesis, and the shear variance, $\langle u_z^2 \rangle$, is obtained by iteratively integrating the reliably resolved portion of the shear wavenumber spectrum of half-overlapping 1-s segments. Narrow band noise peaks induced by a probe guard are above the wavenumber range chosen for the analysis. Typical commonly accepted uncertainty in shear-probe ε measurements is a factor of two (Moum et al., 1995). Dissipation data in the upper 3–4 m (2–3 m below ice) are unreliable due to the initial adjustment to the free fall.

The profiles of precision CTD (corrected against available SeaBird 19 SeaCat CTD profiles) and ε are produced as 10 and 50 cm vertical averages, respectively. A sequence of 4–7 microstructure profiles (set hereafter) was acquired typically around 11:00 and 16:00 UTC between doy = 80–85 and doy = 87–89. The duration of each set was less than 0.5 h. A set ensemble of 50-cm vertical bin averaged dissipation profile thus consists of 8–14 data points when both shear probes acquired acceptable data.

The diapycnal eddy diffusivity is estimated using set averaged $\langle \varepsilon \rangle$ and $\langle N^2 \rangle$ as $K_\rho = 2\nu(\langle \varepsilon \rangle / \nu \langle N \rangle^2)^{1/2}$, valid for $\varepsilon/\nu N^2 > 100$ (Shih et al., 2005). Here and throughout the buoyancy frequency, $N = (-g/\rho \partial\rho/\partial z)^{1/2}$, is calculated using Thorpe-ordered set averaged σ_θ profiles (Thorpe, 1977) with density gradient obtained from the slope of linear fits of $\langle \sigma_\theta \rangle$ against depth in 4 m sliding boxcar windows. The application of this model differs from the common practice of using $K_\rho \leqslant \Gamma\varepsilon/N^2$ (Osborn, 1980), with a typical value of $\Gamma = 0.2$ and is discussed in Section 5.1.

3. Oceanic background: tides, currents and hydrography

The island, Akseløya, across the mouth of the fjord restricts the exchange between the basin and outer coastal water masses to between two sounds: Akselsundet in the north and Mariasundet in the south (Fig. 1). Mariasundet is further divided into two small sounds of 200 m width 2 m depth in the north and 500 m width and 12 m depth in the south. Especially, the northern sound will have negligible influence when covered by the observed 1.2 m thick ice during our experiment. The majority of the exchange takes place at the deeper (sill depth of 34 m) and wider (1.1 km) Akselsundet. The inflowing current is influenced by the Atlantic water and is typically warmer than the basin water. The fjord, at the time of the measurements, is completely covered by ice, which prevents energy input from the wind. At the main entrance Akselsundet, flow is in-fjord during floods and out-fjord during ebbs, reaching

maximum velocities of about 1.5 and 2.5 m s^{-1}, respectively (Bergh, 2004). Depth averaged currents along the principal axis (PA) at the sill in Akselsundet measured by an acoustic Doppler current profiler are within 0.5–1 m s^{-1} for floods and 1–2 m s^{-1} for ebbs during spring tides (Frank Nilsen, personal communication 2006). The linear internal wave speed of the lowest baroclinic mode (first mode) derived from set-mean MSS N^2-profiles varies between 2 and 5 cm s^{-1} at our measurement site, and is in the range 4–18 cm s^{-1} derived from a CTD survey in spring 2002 (Bergh, 2004). A densimetric Froude number, based on the ratio of the depth-averaged current for floods during spring tides and the first-mode internal wave phase speed, will be greater than unity favoring tidal jet formation at the sill. During floods, tidal choking (Stigebrandt, 1980) creates tidal jets with estimated total volume flux of about $(20–30)\times10^3$ m^{3}s^{-1} (Bergh, 2004). The total energy in the jet entering the fjord during one tidal cycle is of order 10^{13} J, partitioned as 1:12 between Mariasundet:Akselsundet (Bergh, 2004). The jet loses only about 1% of its energy to friction (bottom and ice) and is therefore the main driving force for the mean circulation. The loss in generating mid-column turbulence, however, was not evaluated. The tidal jet entering the fjord through Akselsundet is affected by the Coriolis force and rotates cyclonically. For reference, the width of the fjord slightly downstream of Akselsundet is 10 km and the Rossby radii of deformation are 7.5 and 3.75 km, respectively, for jet speeds of 1 and 0.5 m/s. Along the southern coast there is nearly continuous in-fjord flow (Fig. 2b). During ebbs, there is net out-fjord flow along the northern coast (Bergh, 2004). The Coriolis force and the asymmetry of the flow pattern between ebb and flood create a net cyclonic circulation.

The current recorded by RCMs are rotated into along- and across-PA components where PA aligned at 53° clockwise from north, approximately along the coastline. At the station, there is inflow,

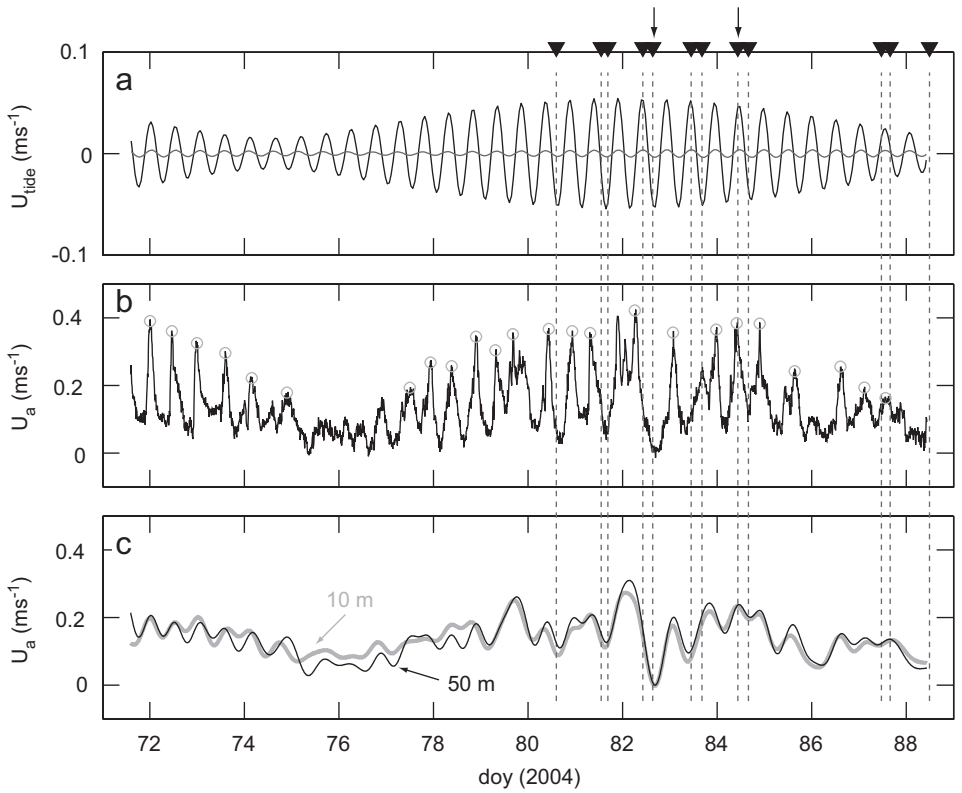

Fig. 2. Time series of (a) tidal current along (black) and across (grey, low amplitude) the principal axis (PA) inferred from harmonic analysis of current recorded at 50 m, (b) along-PA component, U_a, of the velocity at 50 m, and (c) 14-h low-passed U_a at 10 m (grey) and 50 m (black). The arrowheads on top and the vertical dashed lines mark the mean time of deployment of MSS sets. The two MSS sets identified by arrows are shown in detail in Fig. 6. The circles in (b) mark the times of large inflow detected for the mean structure derived in Fig. 9.

i.e. into the fjord, at all times. Along-PA current (U_a) accounted for more than 98% of the total variance and when averaged over the total duration of 16.85 days $U_a = 13.8\,\mathrm{cm\,s^{-1}}$ at both 10 and 50 m depth. The major/minor axis half lengths are $6.8/3.1\,\mathrm{cm\,s^{-1}}$ at 10 m and $8.3/2.8\,\mathrm{cm\,s^{-1}}$ at 50 m, respectively. The total mean horizontal kinetic energy per unit mass is $1.3 \times 10^{-2}\,\mathrm{J\,kg^{-1}}$ averaged over both depths.

Harmonic analysis of hourly averaged currents recorded by the RCMs resolved the semidiurnal constituents (M_2 and S_2) with signal-to-noise ratio greater than 2 at both depths. The tidal amplitude along the PA is $U_{M2} = 0.04\ (\pm 0.02)\,\mathrm{m\,s^{-1}}$ at 50 m for the dominant M_2 constituent. The corresponding tidal excursion amplitude, U_{M2}/ω_{M2}, is 285 ($\pm$142) m using the M_2 frequency $\omega_{M2} = 1.4052 \times 10^{-4}\,\mathrm{s^{-1}}$. Note that at this latitude the inertial frequency $f = 1.425 \times 10^{-4}\,\mathrm{s^{-1}}$ is slightly larger than ω_{M2} and cannot be distinguished in the harmonic analysis. At both levels the resolved semidiurnal components accounted for only ~18% of the along-PA variance. Most of the turbulence profiling was conducted during spring tides (Fig. 2a). Low-passed currents show low-frequency oscillations, particularly during the first part of MSS sets around doy 82–83, when a strong reversal decreases U_a to nearly nil (Fig. 2c). Low-passed currents are correlated with the tidal amplitude (95% confidence interval for the correlation coefficient between the along-PA U_{tide} and low-passed U_a at 50 m is 0.05–0.24), further supporting that the tidal jet forces the mean circulation.

A composite θ–S diagram for all 12 MSS sets show significant variability, although within a narrow range of θ–S values, not directly associated with the tidal cycle (Fig. 3, Section 4.3). The temperatures are always less than $-1.7\,^{\circ}\mathrm{C}$, but are above the freezing point. The spring profiles (sets 1–9) are relatively warmer as a consequence of warmer inflow brought in by the tidal jet. During neaps (the later MSS sets 10–12), the nearly mixed water column is rapidly stratified (set 12). The profiles do not show an obvious mixing line between two water masses and suggest that the hydrography at the site is mainly determined by the dominating advective inflow properties. The salinity is the stratifying agent at all times and the conditions are stable to double diffusion. When derived over all profiles the survey-mean buoyancy frequency is $\langle N^2 \rangle^{1/2} = 1.8 \times 10^{-3}\,\mathrm{s^{-1}}$ or ~1 cycle per hour (cph, $1\,\mathrm{cph} = 2\pi/3600\,\mathrm{s^{-1}}$). The depth of surface mixed layer (D) calculated using the split-and-merge method (Thomson and Fine, 2003) is ~9 m on the average and varies between 3 m (doy = 83.45) and 30 m (doy = 83.68).

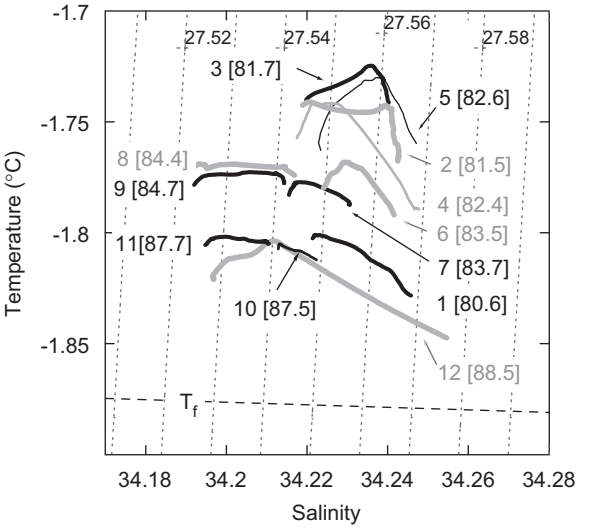

Fig. 3. Potential temperature—salinity diagram for set-averaged MSS profiles. Each set is numbered sequentially from 1 to 12 with corresponding doy indicated in brackets. Traces are in alternating colors of grey and black (except sets 10–11) to ease reading. Dotted contours are isopycnals (σ_θ) and the dashed line shows the freezing temperature, T_f, at atmospheric pressure.

4. Mixing levels

4.1. Mixing in the water column

The dissipation in the water column was typically characterized by enhanced values close to the ice, decreasing with distance from the ice to background values of order $10^{-8}\,\mathrm{W\,kg^{-1}}$ (Fig. 4). Among the microstructure profiles, those conducted on doy = 84.4 were at the time of maximum inflow (larger currents occurred, however, not at the time of MSS profiles, Fig. 5a) and the whole water column was exceptionally turbulent (Fig. 4e). Over all MSS sets, the buoyancy Reynolds number, or turbulent activity index $Re_\rho = \varepsilon/\nu N^2$, spanned five orders of magnitude between 4×10^2 and 4.7×10^7 with a survey-mean of $\langle Re_\rho \rangle = 1.5 \times 10^5$ and all values above the threshold of about 200 when local isotropy is believed to be achieved (Yamazaki and Osborn, 1990). The maximum likelihood estimator (MLE) from lognormal distribution (Baker and Gibson, 1987) of dissipation is $\langle \varepsilon \rangle = 1.1 \times 10^{-7}\,\mathrm{W\,kg^{-1}}$ with 95% confidence intervals of

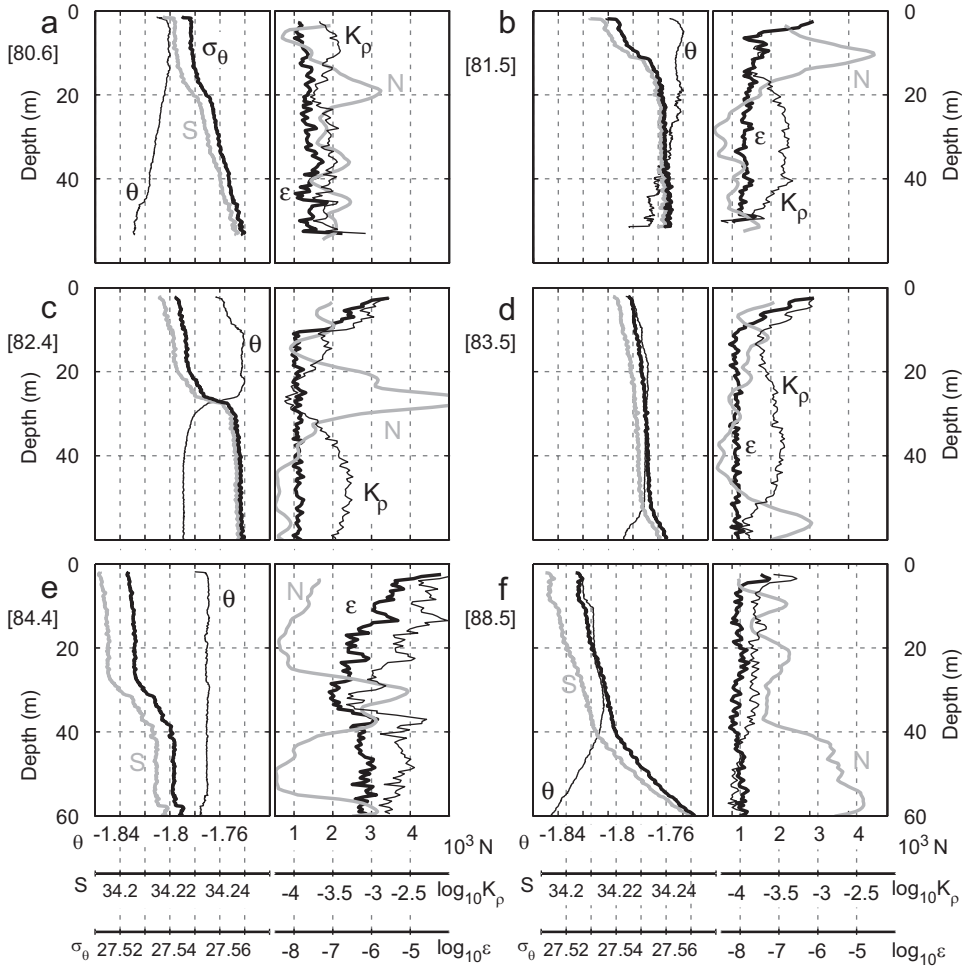

Fig. 4. Representative set averaged profiles of hydrography and mixing at times indicated by the corresponding doy (within brackets). Only the profiles collected near local noon are shown. The profiles of potential temperature, θ (thin black), salinity, S (grey), and σ_θ (thick black) are shown together on the left of each panel ((a)–(f)). The corresponding profiles of dissipation, ε (thick black), vertical diffusivity, K_ρ (thin black), and the $10^3 \times$ buoyancy frequency, N (grey) are shown to the right.

9.8×10^{-8}–$1.2 \times 10^{-7}\,\mathrm{W\,kg^{-1}}$. The values of eddy diffusivity ranged from 7×10^{-5} to $2 \times 10^{-2}\,\mathrm{m^2\,s^{-1}}$ with MLE of $\langle K_\rho \rangle = 7.3 \times 10^{-4}\,\mathrm{m^2\,s^{-1}}$ and 95% confidence intervals of 6.9–$7.8 \times 10^{-4}\,\mathrm{m^2\,s^{-1}}$. The arithmetic average for both ε ($2.2 \times 10^{-7}\,\mathrm{W\,kg^{-1}}$) and K_ρ ($7.8 \times 10^{-4}\,\mathrm{m^2\,s^{-1}}$) are comparable to MLE values. The MLE values of ε and K_ρ are reduced by 44% and 22%, respectively, when the profiles at doy = 84.4 are not included. The survey-mean values are 10–100 times greater than typical values found in the open ocean thermocline (Gregg, 1998) and are comparable to other shelf studies (Section 5.4). The depth averaged total horizontal energy density, $1.3 \times 10^{-2}\,\mathrm{J\,kg^{-1}}$, would be dissipated in 1.5 days, using $\varepsilon = 10^{-7}\,\mathrm{W\,kg^{-1}}$.

The heat flux, $F_\mathrm{H} = -\rho C_\mathrm{P} \langle \mathrm{d}T/\mathrm{d}z \rangle \langle K_\rho \rangle$, profiles are calculated from MSS sets at 5 m moving vertical intervals using only the portions when the vertical temperature gradient was greater than twice its error estimate. The time development of mixing and heat flux in the water column is shown in Fig. 5 together with the hydrography, the observed currents and a representative background bulk shear, $Sh = ((\partial u/\partial z)^2 + (\partial v/\partial z)^2)^{1/2}$, calculated using the RCM currents at 10 and 50 m. Relatively warm patches of water advected by the tidal jet lead to upward heat fluxes of up to $20\,\mathrm{W\,m^{-2}}$. Below a depth comparable to the sill depth at Akselsundet, the temperature typically decreases with depth, yielding negative heat fluxes of comparable magnitude.

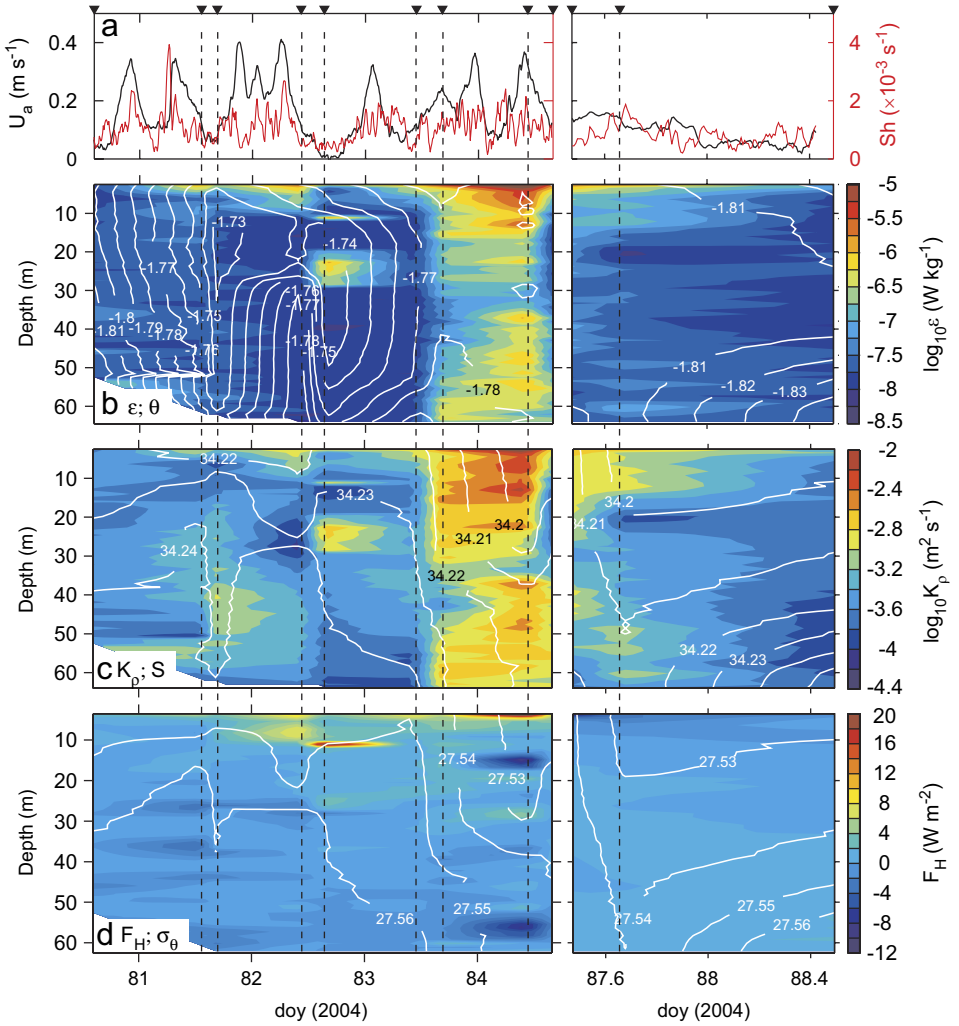

Fig. 5. Time-depth maps of hydrography and mixing together with (a) along-PA component of the current at 50 m (U_a, black, expanded from Fig. 2) and 40-m bulk shear, *Sh* (red) between the current at 10–50 m. Panels are split between doy = 84.66 and 87.47 when there is a long gap in profile measurements. Measurement times are indicated by arrowheads on top and vertical dashed lines; (b) dissipation (color) and temperature (white); (c) vertical diffusivity (color) and salinity (white); and (d) heat flux (color) and σ_θ (white). Profiles are undersampled in time and the linear interpolation between the profiles might not be representative of the actual fields.

Sequences from two selected MSS sets are shown in detail in Fig. 6. Both sets were collected during spring tides, but that on doy 82.6 was during ebb and with the lowest recorded U_a whereas that on doy 84.4 was during flood and with the largest recorded U_a (Fig. 2). The time interval between profiles of each set is about 5 min, however, both the temperature profiles and the microstructure vary substantially. During ebb with low U_a, the microstructure shear is relatively quiescent, but intermittent events (such as that at ~25 m at profile 4) occur which cannot be tracked between subsequent profiles. A mean vertical temperature gradient persists in the upper and lower 20 m of the temperature profiles towards warmer, nearly well-mixed mid-column water. This warm core has low small-scale temperature gradient but is capped by relatively turbulent layers at the top and bottom. During spring tide and large U_a, the temperature profiles are more irregular and variable. In mid-column, warm water appears to advect through the sequence of profiles, mixing the cold core at profile 1 (note the activity in T and dT/dz at profile 2) to a nearly homogeneous column by profile 4 and further leaving a signature of temperature maximum at about 35 m. Compared to doy 82.6,

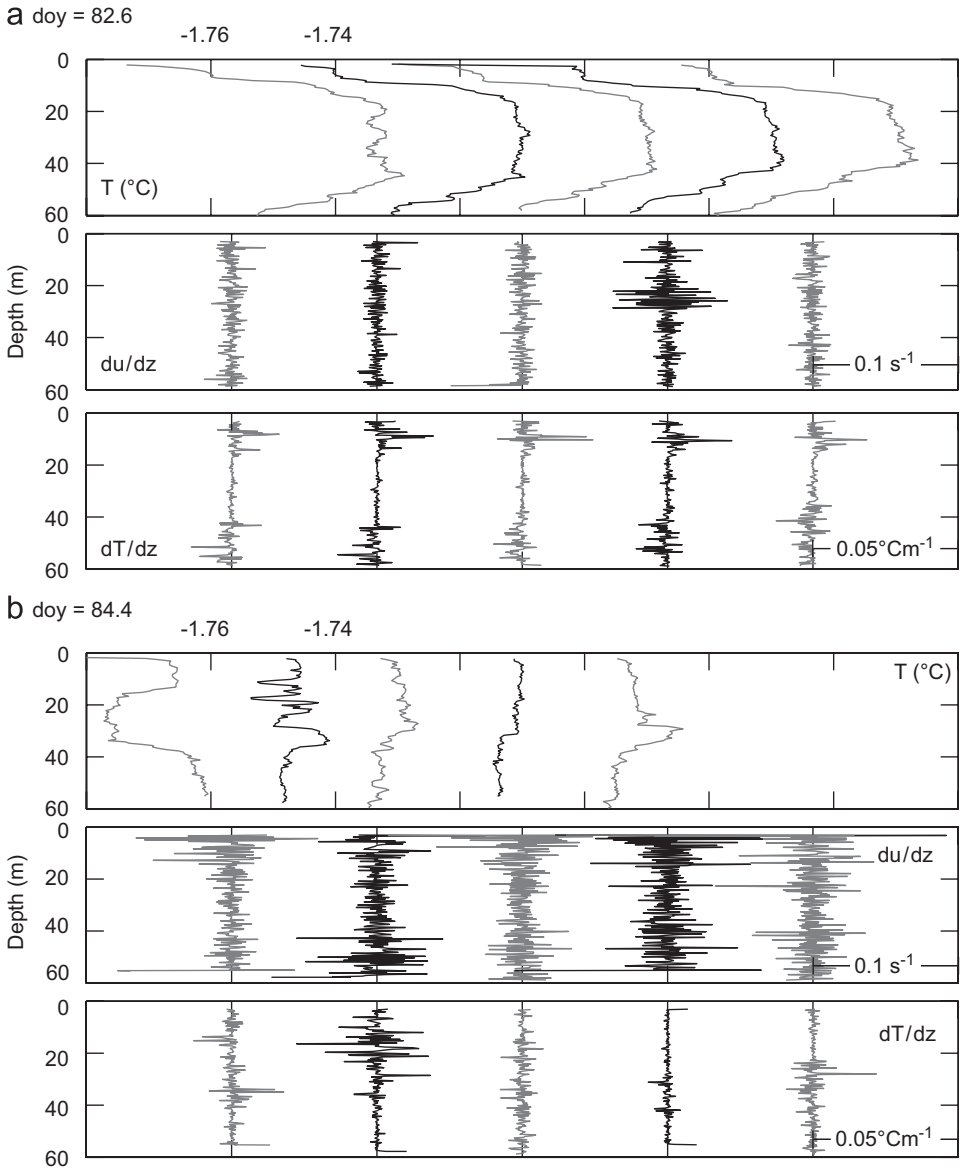

Fig. 6. Sequence of temperature, T, microstructure shear, du/dz, and temperature gradient, dT/dz profiles collected at (a) doy = 82.6 and (b) doy = 84.4. The time of occupation of the two MSS sets are marked by arrows in Fig. 2a. In this representation T profiles are averaged at 0.5 m intervals, microstructure profiles are 4 Hz low-passed and further averaged in 0.5 s (128 scan) bins. Only shear data from one probe are shown, however, both probes recorded consistent features. Subsequent profiles are offset by 0.02 °C (T), 0.1 s^{-1} (du/dz) and 0.05 °C m^{-1} (dT/dz). Axis ranges and scales are identical for corresponding parameters for easy comparison.

microstructure shear is elevated throughout the water column, and particularly in the upper layers close to the ice due to TKE produced by swifter current at the under-ice boundary. Despite the increase in shear levels, the temperature gradient is not exceptionally elevated at doy 84.4, and we note, in general, that patches of turbulent activity in shear and temperature do not often correspond.

4.2. Under-ice boundary heat fluxes

Under-ice boundary layer heat fluxes were directly measured by TICs as 15 min covariances at 1 and 5 m below the ice. The sub-set of F_H time series covering the MSS- deployment period ranges from -8 to 41 W m^{-2}, with a time average of 5 W m^{-2}, towards the ice when averaged over both

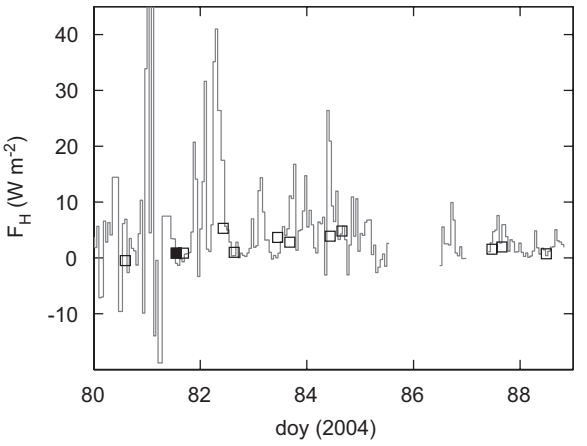

Fig. 7. Time series of oceanic heat flux, F_H, positive upwards towards the ice, measured by TICs (grey trace) and inferred from MSS measurements (squares) at 5 m below the ice. 15-min TIC measurements are averaged over 1 h intervals. MSS data are shown as the averages over 4–6 m below the ice. The filled square is the MSS set where the mean vertical temperature gradient was not greater than twice its error estimate, but is shown for completeness. The value of F_H at doy = 81 measured by TIC is $85\,W\,m^{-2}$.

TICs. This is comparable to the mean conductive heat flux of $\sim 6\,W\,m^{-2}$ in the lower part of the ice. Hourly averages at 5 m, representative of the heat fluxes in the boundary layer, are compared to set-averaged heat fluxes derived from profiler measurements within 4–6 m below the ice (Fig. 7). Large heat flux events correlate with the periods of large U_a (compare Figs. 5a and 7), which can be associated with the tidal jet and its heat content. MSS-set averaged F_H at 4–6 m below the ice agree satisfactorily with the direct measurements at 5 m (Fig. 7). Due to undersampling in time, the majority of large heat flux events are not captured by the profiling. When the data point when the temperature gradient was not significantly different than its error estimate is ignored (filled square in Fig. 7), the agreement between MSS-derived F_H and the TIC segments closest to the MSS deployment is within 10%. We emphasize that we use the K_ρ model suggested by Shih et al. (2005). When the Osborn model is employed, the MSS overestimates F_H by a factor 17, on average.

4.3. Evolution in tidal cycle

The mean evolution in one semidiurnal tidal cycle is derived as follows. Using the harmonic tidal analysis results, we assign the corresponding phase of the dominant lunar semidiurnal tide, ϕ_{M2} at each measurement time (every 1 h for tide prediction, 15 min for TIC sampling, 10 min for RCMs, and the mean deployment time of each MSS set). All ensembles covering the full ϕ_{M2} are then averaged in 20° bins of ϕ_{M2}. For typically log-normal variable such as ε, the MLE value with 95% confidence intervals is calculated. Fig. 8 shows the mean cycle for selected parameters. The floods, defined as in-fjord ($U_{tide} > 0$), are approximately when $\phi_{M2} < 90°$ and $\phi_{M2} > 270°$. The scatter in Fig. 8a represents individual M_2 cycles and cover the spring-neap range. The mean structure of 40 m Sh^2 is of comparable magnitude to N^2 at times of MSS sets, however, the structure in Fig. 8b is informative but not conclusive. Mean vertical gradients of salinity and temperature (shown as contributions to the density gradient, $\alpha dT/dz$ and $\beta dS/dz$, Fig. 8c) do not have a clear signature suggesting advection by the tidal cycle. Throughout the survey the contribution of temperature to the density is negligible and salinity is the stratifying agent. The mean dissipation inferred from the inertial subrange of the vertical velocity fluctuation spectrum derived from TICs is lower at 5 m than at 1 m, consistent with a decrease in shear production of TKE with increasing distance from wall. The rate of working by the Reynolds stress at 1 m below the ice, ρu_*^3, is at least an order of magnitude less than the water column (3–60 m) integrated dissipation rate with no apparent tidal cycle.

The lack of strong correlation between the mixing variables and the inferred M_2-cycle at the measurement site, as well as the fact that the resolved tidal components accounted for only 18% of the variability (Section 3), leads us to examine the mean structure at a window centered at the time of maximum inflow events. The along-PA current data at 50 m is low-passed with a cut-off period of 6 h and demeaned time series is used to detect times of maximum flow (assigned $t = 0$) within each zero (here defined as $2\,cm\,s^{-1}$) crossing. In total, 24 such events are detected (circles in Fig. 2b) and ensembles of relevant data within ± 6 h of each event are extracted. Only seven of 12 MSS sets were within this time window. The average structure is summarized in Fig. 9. On the average, the maximum U_a develops from and decays to ~ 10–$15\,cm\,s^{-1}$ within $t = \pm 2$ h when it reaches a peak value of $\sim 30\,cm\,s^{-1}$. The dissipation inferred from TICs at both levels and the work under ice at 1 m show significant correlation with the ensemble-mean U_a cycle, with an asymmetric structure increasing in the

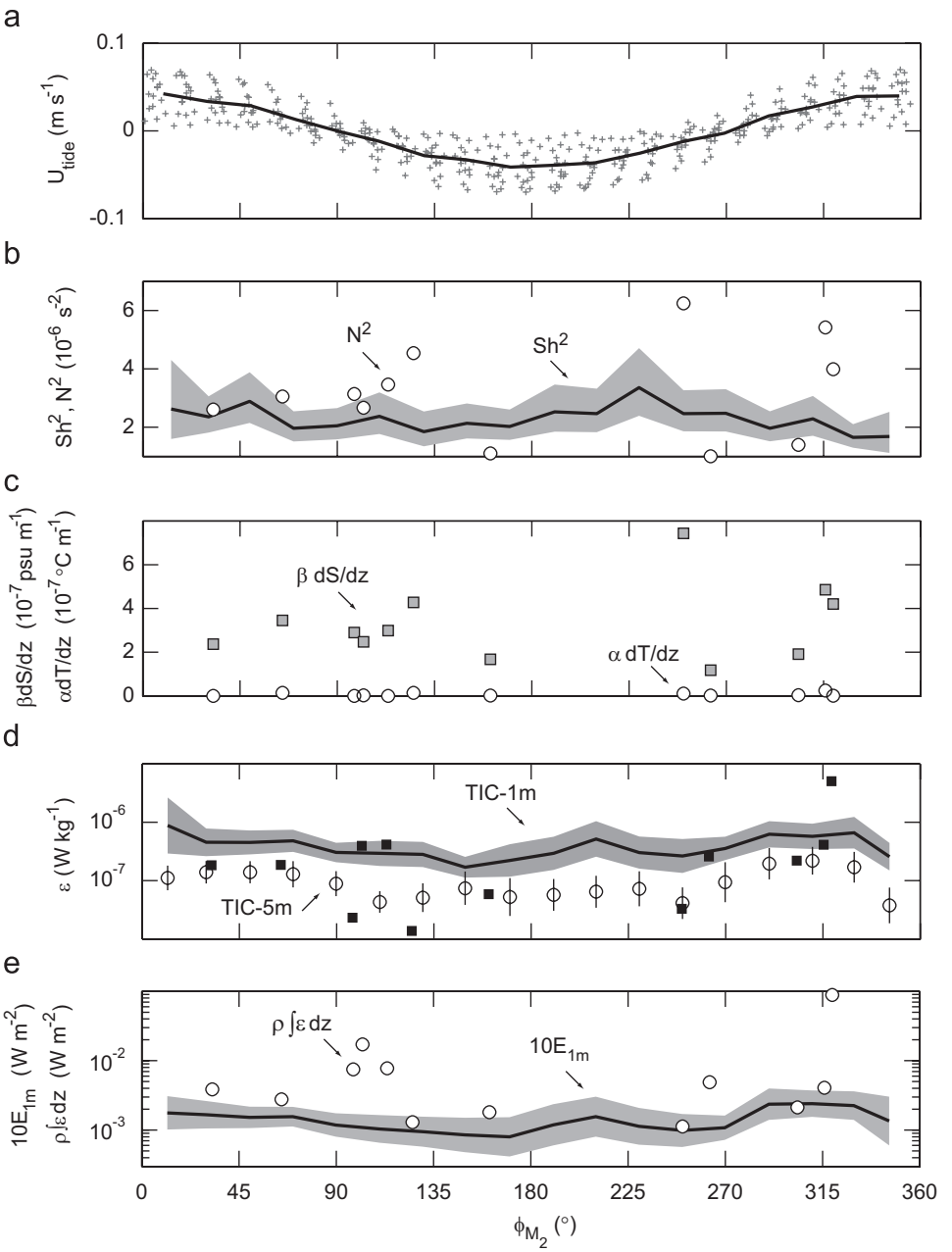

Fig. 8. Properties averaged on M_2 phase, ϕ_{M2}. Continuous time series from RCMs and TICs are averaged into 20° bins of ϕ_{M2}. MSS set averages are shown at the corresponding ϕ_{M2}. (a) Along-PA component of inferred tide at 50 m depth (hourly values, +; ϕ_{M2}-bin averaged, black line); (b) magnitude of shear-squared, Sh^2 between RCMs at 10–50 m (MLE, black line; 95% confidence intervals, grey envelope) and MSS derived squared buoyancy frequency, N^2, for the same depth interval (circles); (c) salinity (grey squares) and temperature (circles) contributions to the vertical density gradient; (d) TIC-derived dissipation at 1 m (MLE, black line; 95% confidence intervals, grey envelope), at 5 m (MLE, circles; 95% confidence intervals, error bars) below the ice and MSS-derived dissipation averaged between 4 and 6 m below the ice (squares); (e) 10 times the work at 1 m below the ice, $E_{1m} = \rho u_*^3$ (MLE, black line; 95% confidence intervals, grey envelope) from TIC and depth integrated dissipation (circles) from MSS sets.

2 h before $t = 0$ and decaying slowly in the subsequent 4 h. There is an apparent phase lag, within 30 min, between the dissipation maximum recorded by the TICs and the maximum U_a at 50 m depth. This is partly due to the different location of the measurement sites: TICs are ~130 m

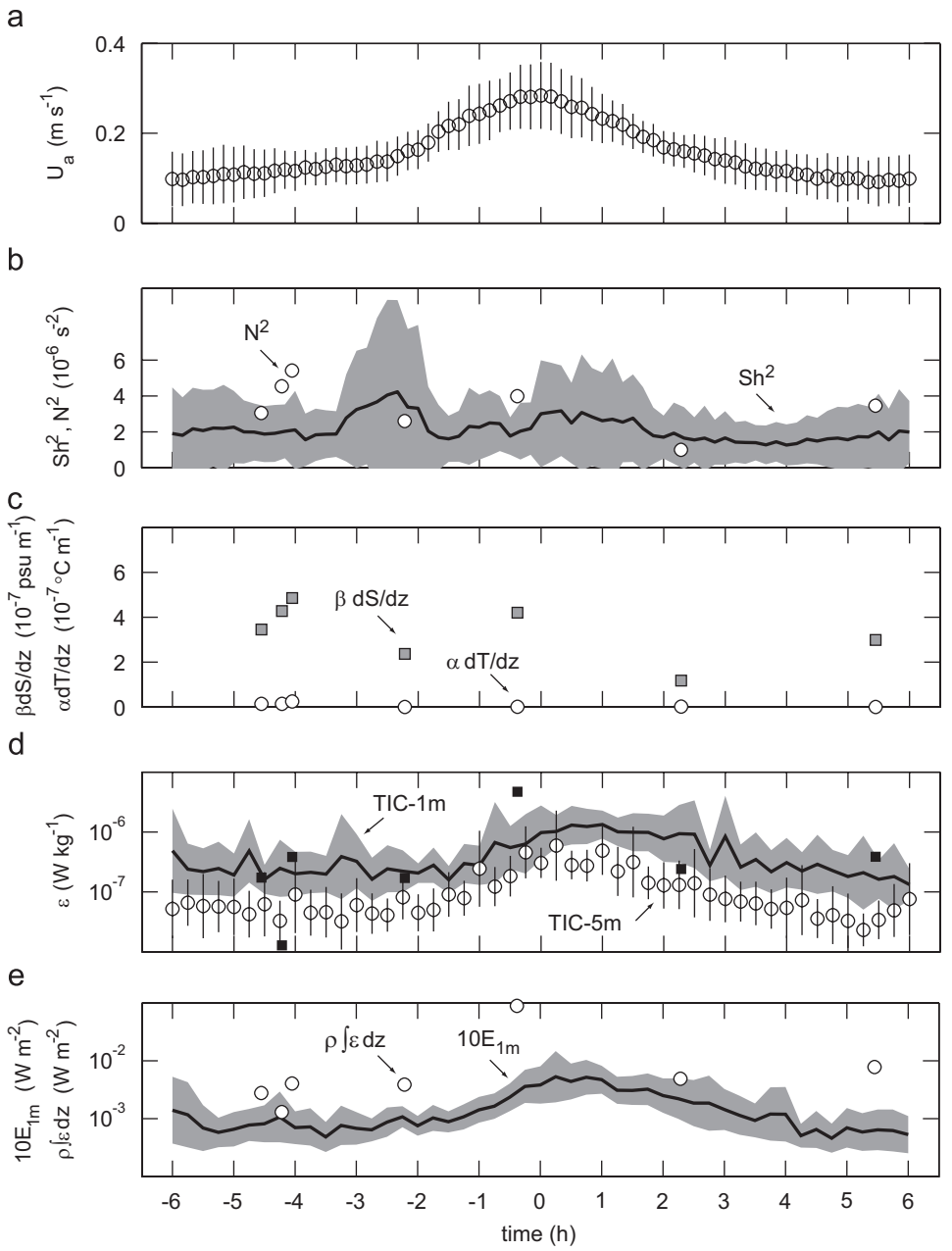

Fig. 9. Same as Fig. 8 but the averaging is done over ensembles of 12-h windows centered at U_a peaks shown in Fig. 2b and panel (a) is the average (error bars = 1 standard deviation) along-PA current at 50 m (instead of tides). Averaged time series from RCMs and TICs are at 10 and 15 min intervals, respectively. MSS data points are placed at the time closest to a U_a peak within ± 6 h (not all sets satisfied this condition).

downstream of the RCMs and the pulse of $U_a \sim 30\,\mathrm{cm\,s^{-1}}$ would take about 7 min to reach the TICs. The speed of the pulse close to the ice where the TICs are located should be less than that at 50 m due to the friction at the under-ice boundary, which can account for the phase lag close to 30 min. Although not significant at 95% confidence level, the shear is slightly elevated at $t = -2$ h when acceleration commences, and shear overcomes stratification at $t \sim \pm 2$ h.

Although tides accounted for only 18% of the variability measured by the RCMs, tides are of major importance due to the jet response of the fjord mouth at Akselsundet. The correlation

between the large inflow events and dissipation is significant (Fig. 9). Such inflow events are generated upstream from the measurement site, in the vicinity of Akselsundet, particularly during spring tides. An examination of Fig. 2b where the inflow events are marked show that such events are quasi-periodic, nearly semidiurnal, and are observed during spring tides. Such periodic events cannot be expected due to external baroclinic forcing.

5. Discussions

5.1. Eddy diffusivity and mixing efficiency

An upper limit for diapycnal eddy diffusivity, K_ρ, is routinely estimated from shear-probe dissipation measurements using the Osborn model $K_\rho \leqslant \Gamma \langle \varepsilon \rangle / \langle N^2 \rangle$ (Osborn, 1980), using a typical value of $\Gamma = 0.2$ (Moum, 1996). The parameter Γ is related to the flux Richardson number, or mixing efficiency, R_f as $\Gamma = R_f/(1-R_f)$. The mixing efficiency is defined as $R_f = F_B/P_S$, where F_B is the buoyancy flux and P_S is the TKE production by mean shear. The buoyancy flux is $F_B = -P_B = g/\rho \langle w'\rho' \rangle$, where P_B is the TKE production by buoyancy, and assuming a steady-state TKE balance of the form $P_S + P_B = \varepsilon$, $R_f = F_B/(F_B + \varepsilon)$, i.e. the ratio of energy loss by working against the stratification to the rate of production by the Reynolds stress in a shear flow. Ellison (1957) found theoretically that a critical maximum value at which the turbulence persists is $R_f = 0.17$, giving $\Gamma = 0.2$. Reports from oceanographic observations are in the range $R_f = 0$–0.3 (Ruddick et al., 1997) and recent studies indicate $R_f = 0.11$ in stably stratified systems with intermittent turbulent patches (Arneborg, 2002) and $R_f = 0.14 \pm 0.04$ for turbulence in the absence of double diffusion (St. Laurent and Schmitt, 1999). Accordingly, the estimates for Γ are highly variable leading to large uncertainties in application of the Osborn model.

Recent laboratory results (Barry et al., 2001) and direct numerical simulations (Shih et al., 2005) showed that for $Re_\rho < 1000$ the Osborn model using $\Gamma = 0.2$ overestimated the measurements by a factor of 2, and for larger Re_ρ the discrepancy systematically increased. For our survey mean $Re_\rho \sim 10^5$, the expected discrepancy is a factor of 32, much larger than the typical factor 4 uncertainty assigned to K_ρ inferred from the Osborn model (Oakey, 1982). When compared with diffusivities (or heat fluxes) from direct eddy-correlation measurements, the Osborn model over-estimated the measurements by a factor 8 in the thermocline at the equator (Moum, 1990) and by a factor of 20 in an estuary (Etemad-Shadidi and Imberger, 2005). Shih et al.'s (2005) data for $Re_\rho = \varepsilon/\nu N^2 > 100$ were best explained by the diapycnal eddy diffusivity $K_\rho = 2\nu(\varepsilon/\nu N^2)^{1/2}$, providing for a novel model as a function of Re_ρ.

The excellent agreement between the direct measurements of the heat flux and that derived from MSS measurements using the Shih et al. (2005) model is encouraging and contributes to the model's validation in an oceanographic setting (Section 4.2). Our data set, however, is severely undersampled and does not allow for more general conclusions. In the marginal ice zone of the Barents Sea, the model suggested by Shih et al. was found to significantly underestimate the eddy diffusivity for heat derived from sufficiently resolved temperature gradient variance and dissipation measurements over 407 turbulent patches (Sundfjord et al., 2007). The mixing efficiency in the Barents Sea marginal ice zone was enhanced due to the presence of double diffusive convection. Mixing efficiency derived from energy budgets of constricted fjord basins, on the other hand, are typically low, in the range of 0.06–0.07 (Stigebrandt, 1999; Arneborg and Liljebladh, 2001) or for an ice-covered fjord 0.003–0.113 (Farmer, 1975). For $Re_\rho \sim 10^5$, the curve fit $R_f = 1.5(Re_\rho)^{-1/2}$ given in Fig. 3 of Shih et al. (2005) yields $R_f \sim \Gamma \sim 0.005$. The success of the Shih et al. model in Van Mijenfjorden can be due to expected low mixing efficiency in a constricted, ice-covered basin with high Re_ρ. Comparably high Re_ρ can be observed in the hot spots of the ocean where enhanced mixing takes place, and the application of the Osborn model with $\Gamma = 0.2$ will considerably overestimate the diapycnal eddy diffusivity.

Using the salt and heat fluxes measured at 1 m below ice, we can calculate the buoyancy flux $F_B = g/\rho \langle w'\rho' \rangle \equiv g\ [\beta \langle w'S' \rangle - \alpha \langle w'T' \rangle]$, and together with the measured dissipation we obtain $R_f = F_B/(F_B + \varepsilon)$, for a steady state TKE budget. Another estimate of shear production is the Reynolds stress squared divided by the eddy viscosity, or using $P_S = u_*^3/\lambda$, where λ is the mixing length scale of turbulence at the measurement level. This gives $R_f = F_B/(u_*^3/\lambda)$. The mixing length is estimated from the wavenumber corresponding to the peak in the variance-preserving w' spectrum (McPhee, 1994). The values of R_f are obtained using both methods. The buoyancy flux, hence R_f, cannot

be calculated at 5 m below the ice due to lack of turbulent salinity flux measurements. Negative values of R_f indicate a destabilizing buoyancy flux whereas those between -1 and 0 indicate that production is dominated by shear. Alternatively, a measure of the effect of surface buoyancy flux is the Monin-Obukhov length, $L_{MO} = u_*^3/(\kappa F_B)$, where $\kappa = 0.4$. As defined, $L<0$ indicates a destabilizing buoyancy flux, and identifies a length scale when the buoyancy terms and shear production terms are of similar importance. When $z/-L_{MO} \gg 1$, buoyancy controls production. Among 232 15 min ensembles with simultaneous F_B, ε and λ values, only two values of R_f were greater than zero with values 1.9 and 129 and two were less than -1 (-1.7 and -2.8). Using the remaining 228 data points the histograms (for $-R_f$ and $-L_{MO}$, to be able to plot on logarithmic scale) are presented in Fig. 10. The distributions are nearly log-normal, which is consistent with previously reported data for stable conditions (Peters and Gregg, 1988; Ruddick et al., 1997). The MLE values are -0.11 and -0.13. For comparison oceanic values of stably stratified shear-generated turbulence are $\langle R_f \rangle = 0.11$ (Peters and Gregg, 1988), $\langle R_f \rangle = 0.15$ (Ruddick et al., 1997) and $\langle R_f \rangle = 0.14$ (St. Laurent and Schmitt, 1999). At 1 m $\langle L_{MO} \rangle = -14.8$ giving $z/-L_{MO} \ll 1$, hence production is dominated by shear. As discussed in Widell et al. (2006), the slightly destabilizing buoyancy flux at 1 m is due to salt release from warming sea ice. Such coherent brine plumes were observed throughout the spring tides when the oceanic heat flux induced by the tidal inflow was significant. No signature of the plumes, however, was found at TIC at 5 m, indicating that the negative buoyancy fluxes and the illustrated R_f and L_{MO} in Fig. 10 are only representative of the surface layer under the ice. An estimate of the buoyancy flux at 5 m below the ice using the salinity flux derived from standard conductivity sensor yields stabilizing buoyancy flux. Although this sensor will underestimate the magnitude of the salt flux (see Section 2.2) the direction of the buoyancy flux is robust. The background stratification in the water column is stable and overall turbulence production is dominated by shear, so we can use the Shih et al. (2005) model devised for stable stratification with some confidence.

5.2. Comparison with relevant work under ice

Crawford et al. (1999) reported on turbulence measurements in the mixed layer under first-year fast ice in Barrow Strait during April–May 1995. Their measurements comprise upper 110 m (45 m above sea bed) microstructure profiles as well as TICs deployed in the under-ice boundary layer. They found energetic turbulence associated with strong currents (sometimes in excess of 20 cm s^{-1}) during springs and an eddy diffusivity proportional to current speed with values up to 2×10^{-2} m^2 s^{-1}, on the average. A strong asymmetry in eddy diffusivity (up to a factor 7) was observed associated with advection of horizontal salinity (density) gradients during the tidal cycle. During the part of the tidal cycle when the mixed layer salinity is decreasing, they identified advection as a process which can create conditions similar to destabilizing

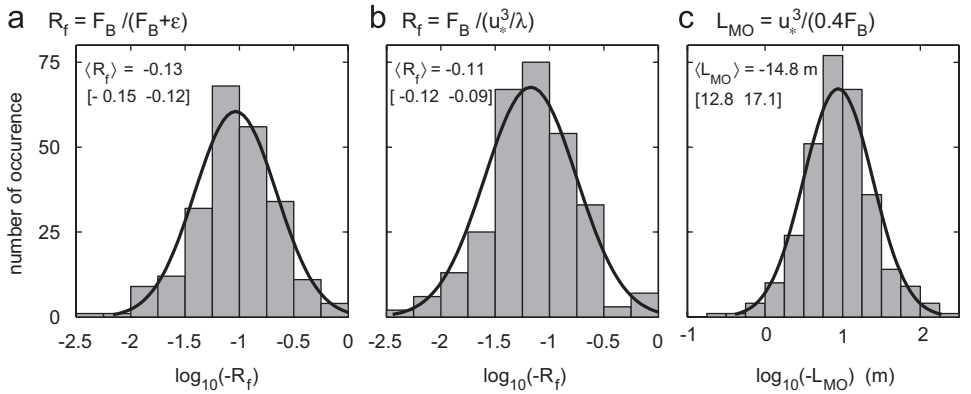

Fig. 10. Histograms of (a) $\log_{10}$-base negative flux Richardson number, R_f at 1 m below ice, using $R_f = F_B/(F_B+\varepsilon)$ and (b) $R_f = F_B/(u_*^3/\lambda)$, where λ is the mixing length and (c) $\log_{10}$-base negative Monin-Obukhov length, $L_{MO} = u_*^3/0.4F_B$, derived over 228 15-min segments. Total number of occurrences are shown in $\Delta\log_{10}(x) = 0.25$ bins (bars). The superimposed curve is the fitted log-normal density. The MLE estimators and 95% confidence intervals (in square brackets) are indicated.

buoyancy flux as if freezing was occurring (the advection close to the ice is retarded due to friction and low salinity water deeper is horizontally advected generating effectively unstable conditions). This is an important observation suggesting an alternative discussion for destabilizing buoyancy fluxes (at 1 m below the ice) recorded in our survey. We did not measure the horizontal density gradients, however, the vertical salinity gradients contributing most to the density structure did not show a clear relation with the tidal cycle (Fig. 8). The time evolution of salinity measured by TICs represents the horizontal gradients in the along-stream direction, however, no indication of tidal advection of salinity gradients was seen.

The under-ice studies by Shirasawa and co-authors (Shirasawa and Ingram, 1991, 1997; Shirasawa et al., 1997) were done using eddy-correlation techniques, similar to TIC deployment, typically 0.5–0.7 m below ice undersurface, with focus on the ocean–ice heat, momentum, exchange. For Resolute Passage they reported a mean oceanic flux of $32\,W m^{-2}$ towards the ice over 12 day sampling period, with a mean eddy viscosity ($K_M \sim O(K_\rho)$) of $\sim 10^{-3}\,m^2\,s^{-1}$, based on measured friction speed of $5.6 \times 10^{-3}\,m\,s^{-1}$ and assuming neutral scaling. The growing thin ice experiment in Saroma-ko Lagoon was of 1 day duration and similar upward heat fluxes ($33\,W m^{-2}$) during non-convective period in the day more than doubled during ice-growth in the night ($K_M = 3.9 \times 10^{-4}$ to $6.5 \times 10^{-4}\,m^2\,s^{-1}$).

In the absence of buoyancy forcing, the eddy diffusivity has been found to scale as $K_\rho = 0.02u_*^2/f$, in the outer (Ekman) part of stratified planetary boundary-layer under drifting sea ice (e.g., McPhee and Martinson, 1994). Here, f is the Coriolis parameter. Using eddy-correlation measurements of heat flux and turbulent stress and the vertical profiles of temperature and velocity, McPhee (1992) reported eddy diffusivities as high as $1.5 \times 10^{-1}\,m^2\,s^{-1}$ in the Ekman layer under drifting ice encountering strong tidal forcing over the Yermak Plateau slope in Fram Strait. In the marginal ice zone of the Barents Sea, average eddy diffusivity in the mixing layer below drifting 1 m thick ice was $\sim 3 \times 10^{-2}\,m^2\,s^{-1}$(Fer and Sundfjord, 2007). In the Ekman layer underneath drifting pack ice during a storm in the Weddell Sea, an eddy diffusivity of around $0.019\,m^2\,s^{-1}$ was reported in McPhee and Martinson (1994). McPhee and Stanton (1996) reported $K_\rho = 5.5 \times 10^{-2}\,m^2\,s^{-1}$ at depths of around 10 m underneath a freezing lead. These results show how forcing by surface buoyancy fluxes during freezing substantially changes the scales of turbulence in the under-ice boundary layer.

The short-term (hourly) heat flux magnitudes presented here of around 2 to $>30\,W m^{-2}$, are roughly comparable to the short-term variability reported in the studies mentioned above. The mean value corresponds fairly well to that encountered underneath drifting ice in the Arctic. Maykut and McPhee (1995) computed the oceanic heat flux from water temperature and drift speed measurements from the AIDJEX experiment in 1975, estimating an annual mean of around $5\,W m^{-2}$ with maximum values in summer in excess of $40\,W m^{-2}$. Their observations further indicated that in the central Arctic, incoming shortwave radiation is the major source of heat to the oceanic heat flux, rather than diffusion from warm water below. During the year-long SHEBA campaign, the oceanic heat flux as estimated from ice temperature and ice mass balance measurements was found to vary over different ice types with a mean for an undeformed multi-year floe of $7.5\,W m^{-2}$ (Perovich and Elder, 2002). Based on drifting buoy temperature and salinity data and u_* computed from satellite ice drift data, Krishfield and Perovich (2005) estimated a basin-wide annual mean value for the Arctic ocean of 3–4 $W m^{-2}$.

Our data were collected in March when the sun angle was low with short daylight, and there were no openings in the ice except at the fjord mouth. We therefore do not expect significant radiative contributions to the under-ice heat balance. The hydrographic data and turbulence measurements indicate that the bulk of the oceanic heat supply stems from upward mixing from the core of inflowing water.

5.3. Comparison with ice-free ocean surface boundary layer

Heat, momentum, and gas exchange between the ocean surface and atmosphere are governed by a combination of processes that can be categorized by those affecting the upper surface layer (e.g., precipitation, surface gravity wave breaking, temperature ramps), those extending below or covering a significant portion of the mixed layer (e.g., convective plumes and Langmuir circulation) and those with manifestations at the base of the mixed layer (inertial shear, Kelvin–Helmholtz instability, internal gravity waves) (Thorpe, 1995; Garrett,

1996; Moum and Smyth, 2001). Anis and Moum (1995) compiled a summary of aquatic surface layer dissipation observations including their measurements. The dissipation rates were sometimes predicted well by law-of-the-wall stress scaling, $\varepsilon_s = u_*^3/\kappa z$ ($\kappa = 0.4$ is von-Karman constant), whereas in other cases there was a discrepancy of more than an order of magnitude, suggested to be due to surface wave-related turbulence. Using data from shear-probe equipped Autosub running at horizontal transects in the upper surface layer, Thorpe et al. (2003) identified breaking waves, bubble clouds, Langmuir circulation and temperature ramps as the principal processes of mixing in the near-surface layer of the ocean. Below a depth of about six times the significant wave height, vertical mixing due to strong Langmuir cells dominated the production of turbulence. The presence of sea ice partially insulates the surface layer from such processes (e.g. surface wave breaking, Langmuir circulation). However, under-ice topography with a broad spectrum of roughness features from millimeter to order 10 m pressure ridge keels can be another source of energy.

Using neutrally buoyant floats at an open ocean site in winter but with weak buoyancy forcing, D'Asaro (2001) measured the vertical velocity variance $\langle w'^2 \rangle$ in the surface layer and compared it with the friction velocity squared, u_*^2. He observed values of $\langle w'^2 \rangle / u_*^2$ 1.75–2 times those measured (approximately unity) for both smooth and rough wall boundary layers driven by shear alone in laboratory experiments (Hinze, 1975) as well as in the under-ice boundary layer (McPhee and Smith, 1976). He attributed this enhanced turbulent vertical kinetic energy to surface wave breaking or Langmuir circulation. By regressing $\langle w'^2 \rangle$ on locally measured u_*^2, we obtain 95% confidence intervals for $\langle w'^2 \rangle / u_*^2$ of [1.3 1.4] at 1 m and [1.6 1.7] at 5 m below the ice in Van Mijenfjorden. At 1 m, TIC is within the constant stress layer and local u_* is representative of the interface value, however at 5 m the above ratio is biased high since we use the local u_* and u_* is expected to decay with distance from the wall. Employing u_* at 1 m, the ratio $\langle w'^2 \rangle / u_*^2$ at 5 m is between 1.2 and 1.3. The 10% increase at 1 m can be associated with the buoyancy input from salt release from the warm ice (Widell et al., 2006), which is negligible compared to the TKE production by shear (Fig. 10). Although the processes suggested by D'Asaro are not at play under fast ice, our observations at 1 m are 30–40% above unity, approximately half the elevation observed in the open ocean boundary layer.

When both wind stress and convection are present, Lombardo and Gregg (1989, LG89) found that the dissipation rate profiles in the oceanic mixed layer were well described when scaled by $1.76\varepsilon_s + 0.58F_B$, where $\varepsilon_s = u_*^3/\kappa z$ is the law-of-the-wall scaling as above and F_B is the surface buoyancy flux. Their dissipation profiles in the mixed layer collapsed to $\varepsilon/(1.76\varepsilon_s + 0.58F_B) = 0.84$. Using the stress and buoyancy flux recorded by TIC at 1 m we evaluate LG89 scaling for both eddy-correlation and MSS measurements (Fig. 11). Lacking the mixed layer depth information at the time of each 15 min TIC segment, we normalized the vertical axis for the survey mean $D = 9$ m for the TIC data. Long time series acquired by the TICs lead to an appropriate averaging over the spring-neap cycle as well as over intermittent turbulent structure and give a statistically significant estimate of the scaling. The MSS profiles, on the other hand, are undersampled in time and are not appropriately

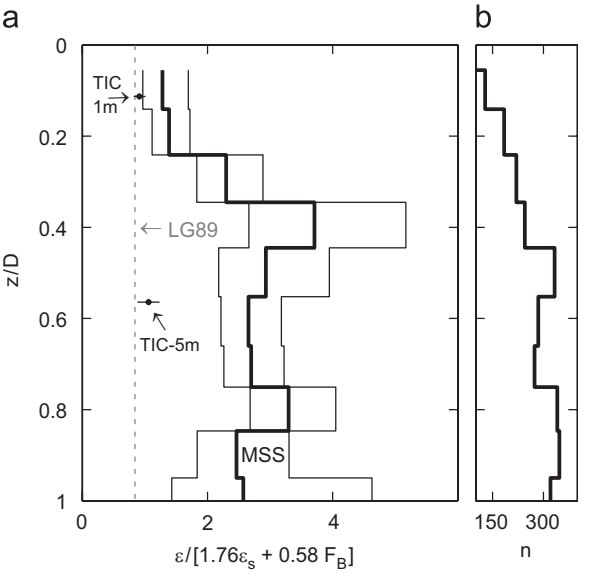

Fig. 11. Profiles of (a) average dissipation, ε, in the mixed layer scaled by $[1.76\varepsilon_s + 0.58F_B]$ suggested in Lombardo and Gregg (1989, LG89) and (b) total number of 0.5-m ε data points (n) used in averaging. Here $\varepsilon_s = u_*^3/0.4z$ is stress scaling and $F_B = w'\rho'$ is the buoyancy flux, each evaluated at 1-m below the ice. The vertical axis is distance below the ice scaled by the mixed layer depth derived for each MSS set. In (a) MLE (thick line) and 95% confidence intervals (thin lines) for MSS are shown for $z/D = 0.1$ bins, vertical dashed line is $\varepsilon/[1.76\varepsilon_s + 0.58F_B] = 0.84$ observed by LG89. Estimators (MLE, dots; 95% confidence intervals, horizontal error bars) for TIC data are shown using a survey mean $D = 9$ m.

representative of the mean turbulent structure. The upper TIC and the MSS estimates at the corresponding level fairly agree both with each other and with LG89 scaling within the measurement uncertainties. The lower TIC at 5 m is slightly above but acceptably close to $\varepsilon/(1.76\varepsilon_s + 0.58F_B) = 0.84$, suggesting LG89 scaling, on the average, is appropriate for the under-ice boundary layer. Below $z/D > 0.25$, MSS measurements indicate dissipation 2–5 times greater than that predicted by LG89. The elevated stirring is possibly to due to "interior" mechanisms and episodic events contributing to the TKE production which cannot be explained by boundary layer processes, however, when sufficient averaging is performed (see TIC at 5 m), the LG89 scaling nearly holds.

5.4. Comparison with other shelf studies

In contrast to the open ocean, there have been few studies reporting on direct turbulence measurements on fjords and shelves. Observations in the Puget Sound fjord, Seattle (WA, USA), show mixing levels $\langle K_\rho \rangle = 1.8\text{–}67 \times 10^{-4}\,m^2\,s^{-1}$, dominated by the passage of a mid-depth density intrusion, possibly related to a strongly advected non-linear tide (Mickett et al., 2004). Enhanced turbulence was associated with shear instabilities as well as double-diffusive layers observed in the warm core of the intrusion. Direct measurements in Storfjorden (Svalbard) in September 2003 (Fer, 2006) showed high levels of background diffusivity of order $10^{-4}\,m^2\,s^{-1}$ which increased by a factor 10 within the density driven bottom-attached overflow of dense, brine enriched fjord waters produced in winter.

Studies of mixing on shelves cover processes associated with the bottom boundary layer (Dewey and Crawford, 1988; Nash and Moum, 2001; Perlin et al., 2005), energetic tidal flows (Rippeth et al., 2003) internal tide, linear and non-linear internal waves and solitons (Sandstrom and Oakey, 1995; Inall et al., 2000; Lien and Gregg, 2001; Rippeth and Inall, 2002; MacKinnon and Gregg, 2003; Moum et al., 2003) and near inertial waves (MacKinnon and Gregg, 2005b). Over smooth continental shelf topography dissipation rate measurements and dye-release experiments show $\langle K_\rho \rangle = 0.1\text{–}5 \times 10^{-5}\,m^2\,s^{-1}$, away from the surface and bottom mixed-layers (Sandstrom and Oakey, 1995; Sundermeyer and Ledwell, 2001; Lozovatsky and Fernando, 2002; MacKinnon and Gregg, 2003; Ledwell et al., 2004), comparable to the open-ocean thermocline. Rough topography and strong forcing, however, enhance turbulent mixing on the shelf and diffusivities typically cover the range 10^{-4} $\text{–}10^{-2}\,m^2s^{-1}$, due to processes associated with proximity to the shelf break, locally generated tides and non-linear internal waves, enhanced energy of high baroclinic modes, instability of low baroclinic modes, shear from near-inertial waves, enhanced bottom drag, etc. (Inall et al., 2000; Nash and Moum, 2001; Mickett et al., 2004; Carter et al., 2005; MacKinnon and Gregg, 2005a, b). The survey mean $\langle K_\rho \rangle = 7.3 \times 10^{-4}\,m^2s^{-1}$ observed in Van Mijenfjorden falls within this range, however, approaches the higher end considering the fact that all cited work employed the Osborn model.

6. Summary and concluding remarks

We described the oceanographic context and reported on water column turbulence observations in early spring 2004 in fast ice covered Van Mijenfjorden. Turbulence measurements were conducted using both moored instruments within the uppermost 5 m below the ice, and a microstructure profiler covering 3–60 m at a water depth of 75 m. While the turbulent fluxes obtained using the eddy-correlation technique (moored instruments) provided excellent sampling in time and covered the spring-neap cycle, the microstructure profiles were few and did not resolve the different phases of the tide. Background currents recorded at two levels, 10 and 50 m, under the ice allowed for neither a detailed analysis of the shear structure nor partitioning of energy into baroclinic modes, but nevertheless gave a description of the bulk currents and tides.

The fjord is characterized as jet type and tidal choking at the mouth of the fjord induces a tidal jet advecting relatively warmer water past the measurement site and dominating the variability in hydrography. The resolved semidiurnal tidal components accounted for only ~18% of the current variance and there was no strong correlation with the observed hydrography or mixing and the M_2 cycle. When conditionally sampled for tidal jet events, the mean structure in dissipation, work done under the ice and the mixing in the water column corresponded to the time development of inflow events.

Observed levels of dissipation, $\langle \varepsilon \rangle = 1.1 \times 10^{-7}$ $W\,kg^{-1}$, and diffusivity, $\langle K_\rho \rangle = 7.3 \times 10^{-4}\,m^2\,s^{-1}$, are comparable to direct measurements at other

coastal sites and shelves with rough topography and strong forcing. During springs, an average upward heat flux of $5\,W\,m^{-2}$ in the under-ice boundary layer was observed. Instantaneous (1 h averaged) large heat flux events were correlated with the periods of large inflow events, hence elevated heat fluxes were associated with the tidal jet and its heat content. The heat flux estimates from microstructure profiler averaged at 4–6 m agreed within 10% with the direct measurements at 5 m below the ice. In deriving heat fluxes from microstructure profiles a novel model for K_ρ (Shih et al., 2005) was employed and our results contributes to the model's validation, however, better sampled field surveys are merited to draw concrete conclusions.

During the experiment destabilizing buoyancy fluxes were recorded at 1 m close to the ice, due to salt release from warm sea ice—especially during the spring tides when the oceanic heat flux induced by the tidal inflow was significant. Overall, the water column was stably stratified and turbulence production was found to be dominated by shear. A scaling of the form $\varepsilon/(1.76\varepsilon_s+0.58F_B)$ (Lombardo and Gregg, 1989) was found to be appropriate for the under-ice boundary layer when judged from well-sampled eddy-correlation results. Microstructure profiles indicated dissipation 2–5 times greater than that predicted by $\varepsilon/(1.76\varepsilon_s+0.58F_B)=0.84$. Because profile data lack the appropriate averaging, the discrepancy is possibly due to bias by episodic events contributing to the TKE production.

Acknowledgements

This work is supported by the Research Council of Norway through projects ProClim (IF) and AiO (KW). Valuable comments and suggestions of Lars Arneborg and Mark Inall are gratefully acknowledged. The authors thank Peter M. Haugan, Miles McPhee, and Frank Nilsen for crucial input to the AiO project and the experiments. This is publication number A166 of the Bjerknes Centre for Climate Research.

References

Anis, A., Moum, J.N., 1995. Surface wave–turbulence interactions: Scaling $\varepsilon(z)$ near the sea surface. Journal of Physical Oceanography 25, 2025–2045.

Arneborg, L., 2002. Mixing efficiencies in patchy turbulence. Journal of Physical Oceanography 32, 1496–1506.

Arneborg, L., Liljebladh, B., 2001. The internal seiches in Gullmar Fjord. Part II: contribution to basin water mixing. Journal of Physical Oceanography 31, 2567–2574.

Baker, M.A., Gibson, C.H., 1987. Sampling turbulence in the stratified ocean: statistical consequences of strong intermittency. Journal of Physical Oceanography 17, 1817–1836.

Barry, M.E., Ivey, G.N., Winters, K.B., Imberger, J., 2001. Measurements of diapycnal diffusivities in stratified fluids. Journal of Fluid Mechanics 442, 267–291.

Bergh, J., 2004. Measured and modelled tidally driven mean circulation under ice cover in Van Mijenfjorden. M.Sc. Thesis, Göteburg University, Göteburg.

Carter, G.S., Gregg, M.C., Lien, R.-C., 2005. Internal waves, solitary-like waves, and mixing on the Monterey Bay shelf. Continental Shelf Research 25, 1499–1520.

Crawford, G., Padman, L., McPhee, M.G., 1999. Turbulent mixing in Barrow Strait. Continental Shelf Research 19, 205–245.

D'Asaro, E., 2001. Turbulent vertical kinetic energy in the ocean mixed layer. Journal of Physical Oceanography 31, 3530–3537.

Dewey, R.K., Crawford, W.R., 1988. Bottom stress estimates from vertical dissipation rate profiles on the continental shelf. Journal of Physical Oceanography 18, 1167–1177.

Ellison, T.H., 1957. Turbulent transport of heat and momentum from an infinite rough plane. Journal of Fluid Mechanics 2, 456–466.

Etemad-Shadidi, A., Imberger, J., 2005. Vertical eddy diffusivity estimations in Swan river estuary. Dynamics of the Atmosphere and Oceans 39, 175–187.

Farmer, D.M., 1975. Penetrative convection in the absence of shear. Quarterly Journal of Royal Meteorological Society 101, 869–891.

Farmer, D.M., Freeland, H.J., 1983. The physical oceanography of fjords. Progress in Oceanography 12, 147–220.

Fer, I., 2006. Scaling turbulent dissipation in an Arctic fjord. Deep-Sea Research II 53, 77–95.

Fer, I., Sundfjord, A., 2007. Observations of upper ocean boundary layer dynamics in the marginal ice zone. Journal of Geophysical Research 112, C04012, doi:10.1029/2005JC003428.

Fer, I., Lemmin, U., Thorpe, S.A., 2002. Observations of mixing near the sides of a deep lake in winter. Limnology and Oceanography 47, 535–544.

Fleury, M., Lueck, R.G., 1994. Direct heat-flux estimates using a towed vehicle. Journal of Physical Oceanography 24, 801–818.

Garrett, C., 1996. Processes in the surface mixed layer of the ocean. Dynamics of the Atmosphere and Oceans 23, 19–34.

Gregg, M.C., 1987. Diapycnal mixing in the thermocline—a review. Journal of Geophysical Research 92, 5249–5286.

Gregg, M.C., 1998. Estimation and geography of diapycnal mixing in the stratified ocean. In: Imberger, J. (Ed.), Physical Processes in Lakes and Oceans. Coastal and Estuarine Studies Series. American Geophysical Union, pp. 305–338.

Hinze, J.O., 1975. Turbulence. McGraw-Hill, New York.

Inall, M., Cottier, F., Griffiths, C., Rippeth, T., 2004. Sill dynamics and energy transformation in a jet fjord. Ocean Dynamics 54, 307–314.

Inall, M.E., Rippeth, T.P., Sherwin, T.J., 2000. Impact of nonlinear waves on the dissipation of internal tidal energy

at a shelf break. Journal of Geophysical Research 105, 8687–8705.

Krishfield, R.A., Perovich, D.K., 2005. Spatial and temporal variability of oceanic heat flux to the Arctic ice pack. Journal of Geophysical Research 110, C07021.

Ledwell, J.R., Duda, T.F., Sundermeyer, M.A., Seim, H.E., 2004. Mixing in a coastal environment: 1. A view from dye dispersion. Journal of Geophysical Research 109, C10013, doi:10.1029/2003JC002194.

Lien, R.-C., Gregg, M.C., 2001. Observations of turbulence in a tidal beam and across a coastal ridge. Journal of Geophysical Research 106, 4575–4591.

Lombardo, C.P., Gregg, M.C., 1989. Similarity scaling of viscous and thermal dissipation in a convecting boundary layer. Journal of Geophysical Research 94, 6273–6284.

Lozovatsky, I.D., Fernando, H.J.S., 2002. Mixing on a shallow shelf of the Black Sea. Journal of Physical Oceanography 32, 945–956.

MacKinnon, J.A., Gregg, M.C., 2003. Mixing on the late-summer New England Shelf—Solibores, shear, and stratification. Journal of Physical Oceanography 33, 1476–1492.

MacKinnon, J.A., Gregg, M.C., 2005a. Spring mixing: turbulence and internal waves during restratification on the New England Shelf. Journal of Physical Oceanography 35, 2425–2443.

MacKinnon, J.A., Gregg, M.C., 2005b. Near-inertial waves on the New England Shelf: the role of evolving stratification, turbulent dissipation, and bottom drag. Journal of Physical Oceanography 35, 2408–2424.

Maykut, G.A., McPhee, M.G., 1995. Solar heating of the Arctic mixed layer. Journal of Geophysical Research 100, 24,691–24,703.

McPhee, M.G., 1992. Turbulent heat flux in the upper ocean under sea ice. Journal of Geophysical Research 97, 5365–5379.

McPhee, M.G., 1994. On the turbulent mixing length in the oceanic boundary layer. Journal of Physical Oceanography 24, 2014–2031.

McPhee, M.G., 2002. Turbulent stress at the ice/ocean interface and bottom surface hydraulic roughness during the SHEBA drift. Journal of Geophysical Research 107, 8037, doi:10.1029/2000JC000633.

McPhee, M.G., Martinson, D.G., 1994. Turbulent mixing under drifting pack ice in the Weddell Sea. Science 263, 218–221.

McPhee, M.G., Smith, J.D., 1976. Measurements of the turbulent boundary layer under pack ice. Journal of Physical Oceanography 6, 696–711.

McPhee, M.G., Stanton, T.P., 1996. Turbulence in the statistically unstable oceanic boundary layer under Artic leads. Journal of Geophysical Research 101, 6409–6428.

Mickett, J.B., Gregg, M.C., Seim, H.E., 2004. Direct measurements of diapycnal mixing in a fjord reach—Puget Sound's main basin. Estuarine and Coastal Marine Science 59, 539–558.

Moum, J.N., 1990. The quest of K_ρ-Preliminary results from direct measurements of turbulent fluxes in the ocean. Journal of Physical Oceanography 20, 1980–1984.

Moum, J.N., 1996. Efficiency of mixing in the main thermocline. Journal of Geophysical Research 101, 12,057–12,069.

Moum, J.N., Smyth, W.D., 2001. Upper Ocean Mixing. In: Steele, J.H., Turekina, K.K., Thorpe, S.A. (Eds.), Encyclopedia of Ocean Sciences. Academic Press, New York.

Moum, J.N., Gregg, M.C., Lien, R.C., Carr, M.E., 1995. Comparison of turbulent kinetic energy dissipation rate estimates from two ocean microstructure profilers. Journal of Atmospheric and Oceanic Technology 12, 346–366.

Moum, J.N., Caldwell, D.R., Nash, J.D., Gunderson, G.D., 2002. Observations of boundary mixing over the continental slope. Journal of Physical Oceanography 32, 2113–2130.

Moum, J.N., Farmer, D.M., Smyth, W.D., Armi, L., Vagle, S., 2003. Structure and generation of turbulence at interfaces strained by internal solitary waves propagating shoreward over the continental shelf. Journal of Physical Oceanography 33, 2093–2112.

Nash, J.D., Moum, J.N., 2001. Internal hydraulic flows on the continental shelf: high drag states over a small bank. Journal of Geophysical Research 106, 4593–4612.

Oakey, N.S., 1982. Determination of the rate of dissipation of turbulent energy from simultaneous temperature and velocity shear microstructure measurements. Journal of Physical Oceanography 12, 256–271.

Osborn, T.D., Lueck, G., 1985. Turbulence measurements from a submarine. Journal of Physical Oceanography 15, 1502–1520.

Osborn, T.R., 1980. Estimates of the local rate of vertical diffusion from dissipation measurements. Journal of Physical Oceanography 10, 83–89.

Perlin, A., Moum, J.N., Klymak, J.M., Levine, M.D., Boyd, T., Kosro, P.M., 2005. A modified law-of-the-wall applied to oceanic bottom boundary layers. Journal of Geophysical Research 110, C10S10, doi:10.1029/2004JC002310.

Perovich, D.K., Elder, B., 2002. Estimates of ocean heat flux at SHEBA. Geophysical Research Letters 29 Art. no. 1344.

Peters, H., Gregg, M.C., 1988. Some dynamical and statistical properties of equatorial turbulence. In: Nihoul, J.C.J., Jamart, B.M. (Eds.), Small-scale Turbulence and Mixing in the Ocean. Elsevier, Amsterdam, pp. 185–200.

Prandke, H., Stips, A., 1998. Test measurements with an operational microstructure turbulence profiler: detection limit of dissipation rates. Aquatic Science 60, 191–209.

Rippeth, T.P., Inall, M.E., 2002. Observations of the internal tide and associated mixing across the Malin Shelf. Journal of Geophysical Research 107, 3028, doi:10.1029/2000JC000761.

Rippeth, T.P., Simpson, J.H., Williams, E., Inall, M.E., 2003. Measurements of the rates of production and dissipation of turbulent kinetic energy in an energetic tidal flow: Red Wharf Bay revisited. Journal of Physical Oceanography 33, 1889–1901.

Ruddick, B.R., Walsh, D., Oakey, N.S., 1997. Variations in apparent mixing efficiency in the North Atlantic Central Water. Journal of Physical Oceanography 27, 2589–2605.

Sandstrom, H., Oakey, N.S., 1995. Dissipation in internal tides and solitary waves. Journal of Physical Oceanography 25, 604–614.

Shih, L.H., Koseff, J.R., Ivey, G.N., Ferziger, J.H., 2005. Parameterization of turbulent fluxes and scales using homogeneous sheared stably stratified turbulence simulations. Journal of Fluid Mechanics 525, 193–214.

Shirasawa, K., Ingram, R.G., 1991. Characteristics of the turbulent oceanic boundary layer under sea ice. Part 2: measurements in southeast Hudson Bay. Journal of Marine Systems 2, 161–169.

Shirasawa, K., Ingram, R.G., 1997. Currents and turbulent fluxes under the first-year sea ice in Resolute Passage, Northwest Territories, Canada. Journal of Marine Systems 11, 21–32.

Shirasawa, K., Ingram, R.G., Hudier, E.J.-J., 1997. Oceanic heat fluxes under thin ice in Saroma-ko Lagoon, Hokkaido, Japan. Journal of Marine Systems 11, 9–19.

St. Laurent, L.C., Schmitt, R.W., 1999. The contribution of salt fingers to vertical mixing in the North Atlantic tracer release experiment. Journal of Physical Oceanography 29, 1404–1424.

Stigebrandt, A., 1976. Vertical diffusion driven by internal waves in a sill fjord. Journal of Physical Oceanography 6, 486–495.

Stigebrandt, A., 1980. Some aspects of tidal interaction with fjord constrictions. Estuarine Coastal and Marine Science 11, 151–166.

Stigebrandt, A., 1999. Resistance to barotropic tidal flow in straits by baroclinic wave drag. Journal of Physical Oceanography 29, 191–197.

Stigebrandt, A., Aure, J., 1989. Vertical mixing in basin waters of fjords. Journal of Physical Oceanography 19, 917–926.

Sundfjord, A., Fer, I., Kasajima, Y., Svendsen, H., 2007. Observations of turbulent mixing and hydrography in the marginal ice zone of the Barents Sea. Journal of Geophysical Research 112, C05008, doi:10.1029/2006JC003524.

Sundermeyer, M.A., Ledwell, J.R., 2001. Lateral dispersion over the continental shelf: analysis of dye release experiments. Journal of Geophysical Research 106, 9603–9621.

Thomson, R.E., Fine, I.V., 2003. Estimating mixed layer depth from oceanic profile data. Journal of Atmospheric and Oceanic Technology 20, 319–329.

Thorpe, S.A., 1977. Turbulence and mixing in a Scottish loch. Philosophical Transactions of the Royal Society of London Series A 286, 125–181.

Thorpe, S.A., 1995. Dynamical processes of transfer at the sea surface. Progress in Oceanography 35, 315–352.

Thorpe, S.A., Osborn, T.R., Jackson, J.F.E., Hall, A.J., Lueck, R.G., 2003. Measurements of turbulence in the upper-ocean mixing layer using Autosub. Journal of Physical Oceanography 33, 122–145.

Turner, J.S., 1973. Buoyancy Effects in Fluids. Cambridge University Press, New York.

Widell, K., 2006. Ice–ocean interaction and the under-ice boundary layer in an Arctic fjord, University of Bergen, Bergen, Ph.D. Thesis.

Widell, K., Fer, I., Haugan, P.M., 2006. Salt release from warming sea ice. Geophysical Research Letters 33, L12501, doi:10.1029/2006GL026262.

Yamazaki, H., Osborn, T., 1990. Dissipation estimates for stratified turbulence. Journal of Geophysical Research 95, 9739–9744.